



Synthesis and characterization of Z-scheme $\text{Ag}_2\text{WO}_4/\text{Bi}_2\text{MoO}_6$ heterojunction photocatalyst: enhanced visible-light photodegradation of organic pollutant

Yushan Si¹ · Yongyang Chen¹ · Miao Xu¹ · Xinyu Zhang¹ · Fenfang Zuo¹ · Qishe Yan¹

Received: 13 August 2019 / Accepted: 21 November 2019 / Published online: 29 November 2019
© Springer Science+Business Media, LLC, part of Springer Nature 2019

Abstract

A series of Z-scheme $\text{Ag}_2\text{WO}_4/\text{Bi}_2\text{MoO}_6$ composites were successfully synthesized by a solvothermal-precipitation method. The crystallization, optical property, morphology properties were studied by XRD, UV–Vis DRS, PL, PT, EIS, BET, and SEM, respectively. The photocatalytic properties of Z-scheme $\text{Ag}_2\text{WO}_4/\text{Bi}_2\text{MoO}_6$ photocatalyst were evaluated by the degradation of methylene blue (MB) under visible-light irradiation. The results have shown that 30% $\text{Ag}_2\text{WO}_4/\text{Bi}_2\text{MoO}_6$ samples possessed the highest photocatalytic activity and superior adsorption capability for methylene blue (MB) with almost complete degradation within 30 min, which was considerably better than pure Bi_2MoO_6 (70%) and Ag_2WO_4 (32%). The enhanced photocatalytic activity can be attributed to the synergistic effect in the $\text{Ag}_2\text{WO}_4/\text{Bi}_2\text{MoO}_6$ composites, lower electron–hole recombination rate, and higher electron–hole separation efficiency. Radical trapping experiments revealed that the $\bullet\text{O}_2^-$ and h^+ were the main active species in catalysis. In addition, the potential photocatalytic mechanism also was discussed based on experimental and characterization results. This work provides a simple method for synthesizing photocatalysts with excellent photocatalytic performance, which has a good prospect in the field of water purification.

1 Introduction

In recent years, the rapid development of industrialization has been accompanied by a series of environmental pollution problems that have seriously hindered the sustainable development of society. The pollution of the water environment is the most serious, and a large number of organic pollutants are discharged into the water body [1, 2]. Methylene blue (MB) as a common organic dye widely used in cosmetic industries, paper, and textile is hard to be degraded in a low concentration by traditional methods. Semiconductor photocatalytic technology has the characteristic of green, non-toxic, technology simple that draws the scholars' widespread attention [3–7]. However, many semiconductors respond only to ultraviolet light, which accounts for only 4% of sunlight, limiting the use of catalysts [8, 9]. The development

of a catalyst that can respond to visible light has a good prospect in the field of water purification.

Bismuth-based semiconductors have been favored by many scholars due to their abundant reserves, narrow band-gap, and catalytic oxidation ability in visible light, including BiVO_4 [10–12], BiOX [7, 13–15], Bi_2WO_6 [16, 17], Bi_2O_3 [12, 18], Bi_2MoO_6 [19, 20], etc. Among them, Bi_2MoO_6 , as an important typical Aurivillius phase, has a special perovskite layered structure (Bi_2O_2) ($\text{A}_{m-1}\text{B}_m\text{O}_{3m+1}$) and Bi_2MoO_6 is a direct semiconductor material with an appropriate forbidden bandgap (ca. 2.6 eV) [21, 22], which has good absorption of both ultraviolet light and visible light [23], stable properties and controllable morphology, attracting the attention of most researchers. However, the photocatalytic activity of pure Bi_2MoO_6 is reduced by the rapid recombination of electron–holes. At present, Bi_2MoO_6 is modified by the following methods: coupling with carbon materials, elemental doping, constructing of heterojunction with various other semiconductors. In the above method, the configuration of the heterojunction is one of effective methods for improving the photocatalytic performance. Such as $\text{Ag}_3\text{PO}_4/\text{Bi}_2\text{MoO}_6$ [24], $\text{Ag}/\text{Ag}_2\text{CO}_3/\text{Bi}_2\text{MoO}_6$ [25], $\text{Bi}_2\text{MoO}_6/\text{g-C}_3\text{N}_4$ [26], $\text{Bi}_2\text{MoO}_6/\text{BiOBr}$ [27, 28], $\text{Ag}/\text{AgCl}/\text{Bi}_2\text{MoO}_6$ [29]. Constructing heterojunction is a good way to

✉ Qishe Yan
qisheyanzzu@163.com

¹ Institution of Chemistry and Molecular Engineering,
Zhengzhou University, No. 100, Science Avenue,
Zhengzhou City, Henan Province, China

improve photocatalytic activity. However, the construction of traditional heterojunction type reduces the redox ability of photo-induced electrons–holes. While the Z-scheme not only inherits the excellent charge separation efficiency of traditional heterojunction type but also improves the redox ability of photo-induced carriers.

Recently, a variety of Ag-based semiconductor photocatalyst including AgX (X = Cl, Br, I) [29–32], Ag₃PO₄ [24, 33], Ag₂CO₃ [11], Ag₂MoO₄ [34], etc., has been widely explored, due to their perfect activities in the field of photocatalytic degradation of organic pollutants. Among them, Ag₂WO₄ has a bandgap about 3.1 eV, which has a certain degradation effect on organic pollutants under visible-light irradiation [35, 36]. However, pure Ag₂WO₄ is easy to agglomerate and has a relatively large volume. Combining with other semiconductors can effectively reduce agglomeration and thus enhance photocatalytic activity [36]. The bandgap of Ag₂WO₄ matches well with Bi₂MoO₆ and there are few studies on the preparation of heterogeneous photocatalyst Ag₂WO₄ and Bi₂MoO₆.

In this paper, a series of Z-scheme Ag₂WO₄/Bi₂MoO₆ composites were successfully synthesized by a solvothermal-precipitation method. The crystallization, optical property, morphology properties were studied by XRD, UV–Vis DRS, PL, PT, EIS, BET, and SEM, respectively. The photocatalytic activities of Ag₂WO₄/Bi₂MoO₆ composites were evaluated by the degradation of methylene blue (MB) under visible-light irradiation. The results show that the Ag₂WO₄/Bi₂MoO₆ composites possess higher photocatalytic activity than pure Ag₂WO₄ and Bi₂MoO₆. Radical trapping experiments revealed that the •O₂[−] and h⁺ were the main active species in the photocatalytic degradation process and the possible mechanism was explored.

2 Experimental

2.1 Chemical materials

All the chemicals are analytical grade reagents (purity ≥ 99%) and without further purification, sodium molybdate dihydrate (Na₂MoO₄·2H₂O), bismuth nitrate pentahydrate (Bi(NO₃)₃·5H₂O), sodium tungstate dehydrate (Na₂WO₄·2H₂O), silver nitrate (AgNO₃), ethylene glycol (EG), ethanol and other chemicals bought from Tianjin Kermel Chemical Reagents Factory.

2.2 Preparation of photocatalysts

2.2.1 Preparation of Bi₂MoO₆

Microsphere structural Bi₂MoO₆ was successfully synthesized a simple solvothermal method [29]. AgNO₃,

Bi(NO₃)₃·5H₂O, and Na₂MoO₄·2H₂O were used as the silver, bismuth, and molybdenum precursors, respectively. Briefly, 1.6866 g Bi(NO₃)₃·5H₂O and 0.4210 g Na₂MoO₄·2H₂O were dissolved into 5 mL EG solution, respectively, with stirring to form a transparent solution. Then Na₂MoO₄·2H₂O solution was added slowly into the Bi(NO₃)₃·5H₂O solution under vigorous stirring conditions, and 20 mL of ethanol was slowly dropped into the mixture, followed by stirring to form a clear solution. Thereafter, the mixture was transferred into a 100 mL Teflon-lined stainless steel autoclave, which was heated at 160 °C for 24 h. Then the obtained product was centrifuged, washed with deionized water and ethanol three times, respectively. Finally, dried at 60 °C for one night, pure Bi₂MoO₆ was obtained, which was named as BMO.

2.2.2 Preparation of Ag₂WO₄/Bi₂MoO₆

0.2 mmol (0.122 g) BMO was dissolved in 50 mL deionized water with stirring for 30 min, which was named A solution. 0.08 mmol (0.0136 g) AgNO₃ was dissolved in 5 mL deionized water with stirring until dissolved. The solution was added dropwise into A solution with stirring for 30 min, which was named B solution. 0.04 mmol (0.0132 g) Na₂WO₄·2H₂O was dissolved in 5 mL deionized water; the solution was added dropwise into B solution with stirring for 2 h. Then the obtained product was centrifuged, washed with deionized water and ethanol three times, respectively. Finally, dried at 60 °C for a night, 20% Ag₂WO₄/Bi₂MoO₆ was obtained, which was named as 20% AW/BMO. Adjusted the mole ratio (AW/BMO, 30% wt, 40% wt) with conditions remain unchanged, named as 30% AW/BMO, 40% AW/BMO, respectively. The pure Ag₂WO₄ was prepared without BMO precursor under the same method, which was named as AW.

2.3 Characterization

The X-ray diffraction (XRD) data came from Bruker D8 advanced diffractometer using a Cu Kα radiation to analyze the crystal phases. The morphologies were investigated by scanning electron microscopy (SEM). The specific surface area was characterized by the nitrogen absorption data and Brunauer–Emmett–Teller (BET) measurement (Micromeritics, ASAP 2420). The UV–Vis DRS was recorded by a spectrophotometer (Cary-5000). Photoluminescence (PL) spectra were measured on the F-4600 fluorescence spectrophotometer with an excitation wavelength at 487 nm. Electrochemical properties of the as-prepared samples were determined on a conventional three-electrode, single-compartment quartz cell on a CHI 660E Electrochemical Workstation.

2.4 Photocatalytic properties

The photocatalytic activities of the as-prepared samples were evaluated using a 300 W Xe lamp ($\lambda \geq 400$ nm), and methylene blue (MB) was chosen as a model contaminant. During each photodegradation process, 50 mL of MB (10 mg/L) was mixed with 30 mg of the as-prepared samples. The suspension was constantly stirred 20 min in the dark to ensure the system reach the absorption–desorption equilibrium prior to irradiation. During the illumination process, 3 mL of solution was collected and filtered at the same time interval (10 min); then the concentration of MB was tested by UV–visible spectrophotometer (Shimadzu UV-2450).

The degradation efficiency of SD-Na and residual of longlived organic intermediates in the solutions were measured by chemical oxygen demand (COD).

The mineralization of MB was measured by chemical oxygen demand (COD) [37–39]. The concentration of COD infiltrate was measured by potassium dichromate method: a certain amount of filtrate was diluted with water to 20.00 mL and placed in a 250 mL reflux bottle. 10.00 mL (0.025 mol/L) potassium dichromate standard solution and 30 mL Silver sulfate catalyst were added to the above solution, heated to boiling, and refluxed for 2 h. After cooling to room temperature, three drops of the Ferroin indicator solution was be added and titrated with ammonium ferric sulfate standard solution. The blank test was being done under the same conditions.

In the quenching experiments, 1,4-benzoquinone (BQ), isopropanol (*t*-BuOH), ammonium oxalate ((NH₄)₂C₂O₄) were introduced to the reaction system as scavengers for oxidative free radicals (O₂^{•-}), hydroxyl radical (•OH), holes (h⁺), respectively.

3 Results and discussion

3.1 Morphology and structure analysis

3.1.1 XRD analysis

The XRD patterns of AW, BMO, and AW/BMO with the region of 10–90° are shown in Fig. 1. The characteristic peaks at $2\theta = 10.9^\circ, 28.3^\circ, 32.5^\circ, 32.6^\circ, 33.1^\circ, 36.0^\circ, 46.7^\circ, 47.0^\circ, 55.5^\circ, 56.2^\circ, 76.0^\circ,$ and 78.0° are in good agreement with (020), (131), (200), (002), (060), (151), (202), (062), (133), (191), (193), and (214) crystal planes of orthorhombic BMO (JCPDS No. 72-1524). The peaks of AW at 2θ values of $26.93^\circ, 31.7^\circ, 33.2^\circ, 47.6^\circ, 50.7^\circ, 55.5^\circ, 65.4^\circ, 76.1^\circ,$ and 78.5° can be attributed to (022), (113), (222), (224), (115), (044), (246), and (355) crystal planes of hexagonal AW (JCPDS No. 33-1197),

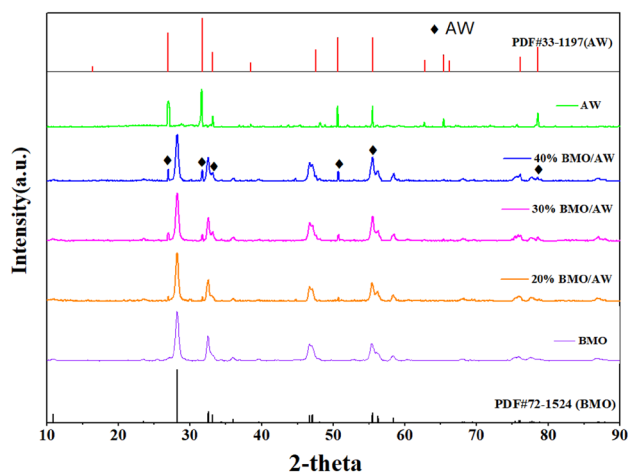


Fig. 1 XRD patterns of AW, BMO, and AW/BMO composites

Table 1 Comparison of average crystallite sizes of AW, BMO and AW/BMO compounds

Samples	β [°] (FWHM)	Mean crystal size [nm]
AW	0.189 (113)	≈ 43.7
40% AW/BMO	0.426	≈ 19.2
30% AW/BMO	0.438	≈ 18.7
20% AW/BMO	0.464	≈ 17.6
BMO	0.487 (131)	≈ 16.8

respectively, that means pure BMO and AW were successfully synthesized. As for the diffraction peaks of AW/BMO composites, all peaks are well-matched to the orthorhombic phase BMO and hexagonal phase AW, no impurity peaks appeared, indicating that the crystalline phases of the AW and BMO did not change and AW/BMO heterojunction photocatalyst was successfully synthesized. Comparatively, the intensities of the corresponding diffraction peaks of AW enhanced gradually along with the increase in the AW contents in the AW/BMO composite.

Furthermore, Debye-Scherrer's formula was used to calculate the crystallite size (D) of as-samples according to the XRD pattern [40–43].

$$D = \frac{0.9\lambda}{\beta \cos \theta}$$

where λ , β , and θ are the wavelength of X-ray (=0.154 nm), the full width at half maximum (FWHM), and the Bragg angle, respectively. The calculated results are displayed in Table 1. Obviously, the crystal size is gradually increasing with the increase in the AW contents, indicating that heterogeneous junction is formed between AW and BMO.

3.1.2 SEM analysis

The morphology of microsphere structural BMO, AW, and 30% AW/BMO have been investigated by SEM. As shown in Fig. 2a, the morphology of pure BMO is a regular three-dimensional hierarchical flowerlike hollow spheres architecture with a diameter of 1–2 μm , which were assembled by serried nanosheets. The special polyporous structure provides BMO a large specific surface area and more adsorption and catalytic sites. It can be seen from Fig. 2b that the size of the rod-shaped AW is relatively large and the size is not uniform. However, AW was deposited more uniformly on the surface of BMO when AW/BMO heterojunction is formed,

which can be seen clearly from the SEM images of 30% AW/BMO (Fig. 2c, d). It may be due to the formation of heterogeneous junctions between AW and BMO, which reduces AW reunion and improves AW/BMO photocatalytic activity.

3.1.3 BET analysis

The pore structure and specific surface area of the as-prepared samples were studied by the nitrogen adsorption–desorption isotherms. From Fig. 3a, we could see the isotherms of BMO and 30% AW/BMO can be ascribed as a classical type IV with an H_3 hysteresis loop according to IUPAC classification, suggesting the formation of mesoporous and the

Fig. 2 SEM images of **a** BMO, **b** AW and **c**, **d** 30% AW/BMO composite

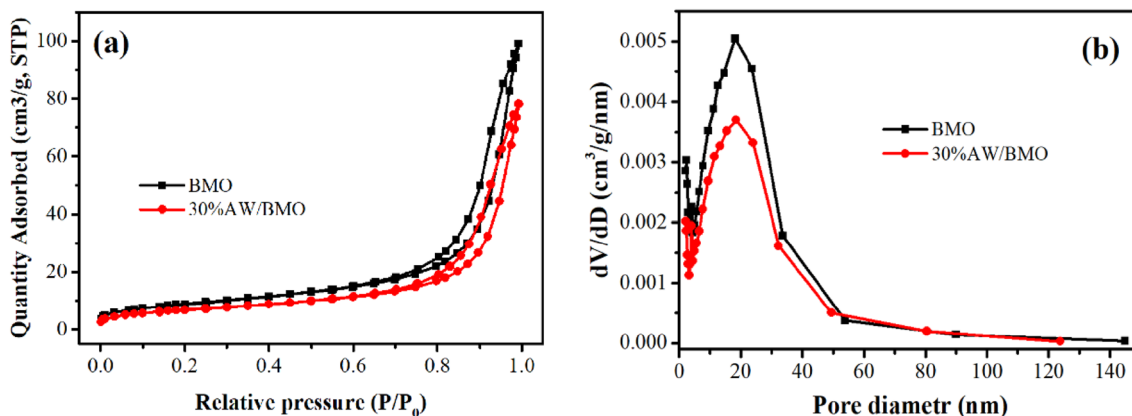
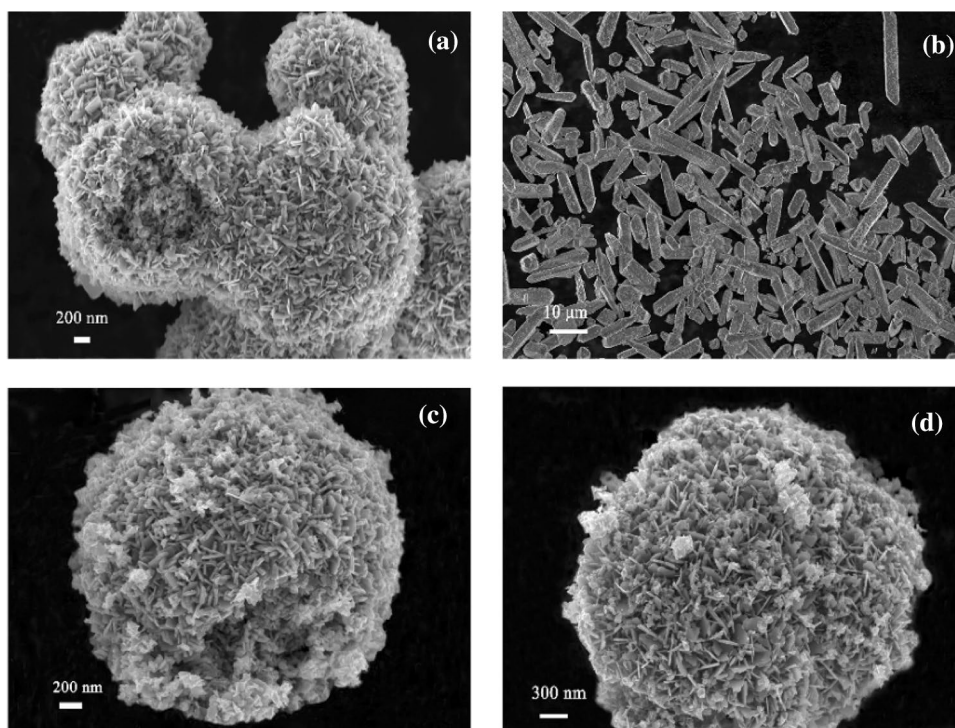


Fig. 3 **a** N_2 adsorption–desorption isotherms and **b** pore size distribution of BMO and 30% AW/BMO samples

existence of slit-shaped pores in the structure. As shown in Fig. 3b, the pore sizes of BMO and 30% AW/BMO are almost within the range of 2–40 nm within the mesoporous region. The average pore sizes of BMO and 30% AW/BMO are 16 nm and 17 nm (Table 2), respectively. The total pore volume and specific surface area of 30% AW/BMO were 0.13 cm³/g and 25 m²/g (Table 2), slightly lower than that of pure BMO (0.16 cm³/g, 32 m²/g), possibly because a large amount of AW was deposited on the surface of BMO, resulting into the blocking of pores [44].

3.2 Optical properties

3.2.1 UV–Vis analysis

The optical properties of BMO, AW, and AW/BMO composites were studied by UV–Vis DRS. As shown in Fig. 4a, the absorption edge of pure AW is approximately 422 nm, indicating that it can absorb light less than 422 nm. Meanwhile, the microspheres BMO had well visible-light absorption with wavelengths shorter than 620 nm. Compared with AW and BMO, the absorption edge of AW/BMO composites (700 nm) shows a red-shifted, indicating that the AW/BMO composites possess better visible-light response-ability. This may be one of the reasons for improving photocatalytic activity because the formation of AW and BMO heterojunction expands the absorption range of visible light.

Table 2 Specific surface area, pore volume, and pore size of BMO and 30% AW/BMO

Samples	Surface area (m ² /g)	Pore volume (cm ³ /g)	Pore size (nm)
BMO	32	0.16	16
30% AW/BMO	25	0.13	17

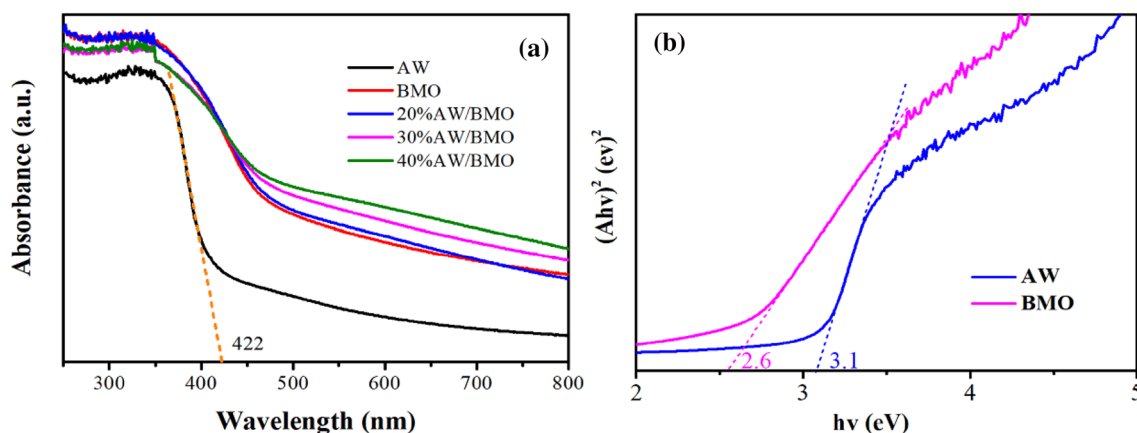


Fig. 4 **a** UV–Vis spectrum of AW, BMO and AW/BMO composites and **b** the bandgap of pure AW and BMO

The bandgap of the photocatalytic semiconductor materials could be calculated followed by the Kubelka–Munk transformation [45]:

$$(\alpha * h * \nu)^{1/n} = A(h * \nu - E_g) \quad (1)$$

where E_g , h , ν , A , and α are the bandgap energy, the Planck's constant, the light frequency, a constant, and the absorption coefficient, respectively. Indirect bandgap semiconductor: $n = 2$, direct bandgap semiconductor: $n = 1/2$, BMO, AW are direct bandgap semiconductors, the values of n are $1/2$. Thus, the E_g of AW and BMO can be calculated as 3.1 eV and 2.6 eV.

3.2.2 PL analysis

The recombination rate of electron–hole pairs was studied by the PL emission method. Generally, the semiconductor with lower fluorescence intensity corresponds to the less recombination of the photo-generated electron–hole pairs, thus leading to a higher photocatalytic activity. As displayed in Fig. 5, the PL spectra of BMO, AW, 30% AW/BMO compounds were excited under a wavelength of 487 nm. The 30% AW/BMO composite exhibits obviously weaker than pure BMO and AW. This indicated that the formation of AW/BMO heterojunction could effectively inhibit the recombination of electron–hole pairs, possibly because the introduction of AW provided more electron–hole capture sites, which is one of the main reasons for enhancing photocatalytic activity.

3.3 Electrochemical property

The separation and transfer efficiency of electron–hole pairs are the key factors affecting photocatalytic activity. The photocurrent value indirectly reflects the separation efficiency of the photo-generated charge carriers. The higher

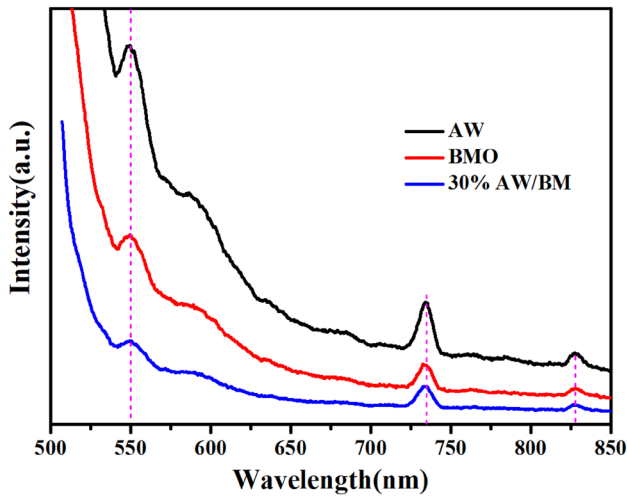


Fig. 5 Photoluminescence spectra of the AW, BMO and 30% AW/BMO composite excited at 487 nm

photocurrent intensity, the more efficient the hole pair separation. The photocurrent response of AW, BMO, 30% AW/BMO is shown in Fig. 6a. The 30% AW/BMO composite showed a higher photocurrent response than the pure AW and BMO, suggesting that the 30% AW/BMO possessed a higher photocatalytic activity. The charge transfer rate on the electrodes was researched by EIS. Generally, the smaller arc in the EIS, the smaller charge-transfer resistance. The EIS changes of AW, BMO, 30% AW/BMO electrodes are shown in Fig. 6b. Clearly, in comparison with pure AW and BMO, the radius of the arc in the EIS spectrum of 30% AW/BMO was smaller, indicating a faster separation and transfer of photo-generated charge carriers, resulting in higher photocatalytic activity.

3.4 Photocatalytic activity

The photocatalytic activity of a series of AW/BMO samples was investigated for the degradation of MB under visible-light illumination ($\lambda \geq 400$ nm). As presented in Fig. 7a, the suspension was constantly stirred 20 min in the dark to ensure the system reach the absorption-desorption

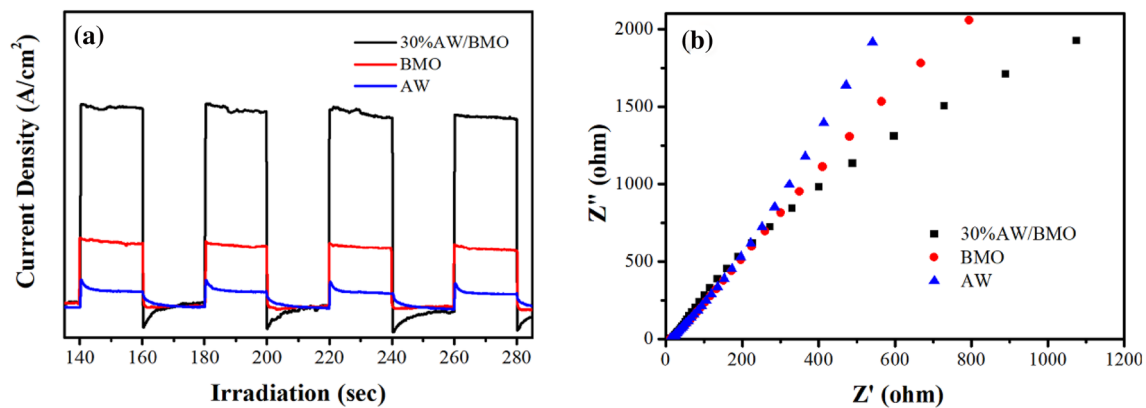


Fig. 6 a photocurrent responses and b the corresponding EIS spectra of AW, BMO and 30% AW/BMO samples

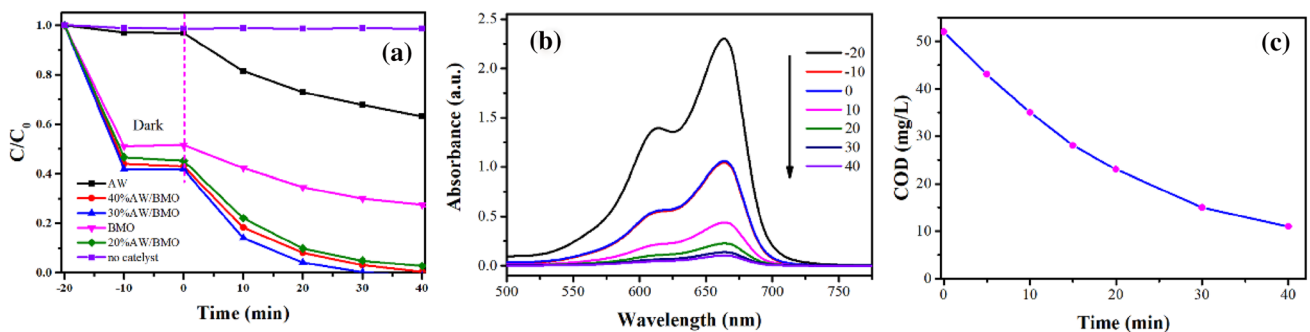


Fig. 7 a The Photocatalytic curves of MB under visible light; b Absorption spectra of the MB at different degradation times using 30% AW/BMO; c variation of COD values of MB

equilibrium prior to irradiation. During the irradiation, the AW/BMO series compounds display excellent photocatalytic activity compared with single BMO and AW for MB degradation. For pure BMO, the degradation rate was 70% after 30 min and the degradation rate of AW is about 45%, while 30% AW/BMO compounds can almost completely degrade MB within 30 min. Figure 7b shows the absorption spectrum of MB (10 mg/L) aqueous solution within 30 min of visible-light irradiation with 30% AW/BMO. As the irradiation progresses, the main absorption peak of MB decreases gradually at 670 nm. About 95.8% of the MB was adsorbed in a dark reaction of 20 min, and almost all of the MB degraded in 40 min. The mineralization of MB was measured by chemical oxygen demand (COD). As shown in Fig. 8c, the values of COD decrease from 52 to 9 mg/L. The COD removal efficiency reached 82.7%, indicating that the synthesized AW/BMO photocatalyst was promising.

3.5 Photocatalytic mechanism

It is well known that h^+ , $\bullet OH$, $\bullet O_2^-$ are considered as the most important active groups in the photocatalytic degradation of organic compounds. To further reveal the photocatalytic mechanism in the degradation process of MB on 30% AW/BMO photocatalyst under visible light, several major active groups were investigated via adding quenchers. In this paper, three different quenchers, ammonium oxalate (AO), 1, 4-benzoquinone (BQ), and isopropanol (IPA), were chosen to quench h^+ , $\bullet O_2^-$, and $\bullet OH$, respectively. As shown in Fig. 8, it can be found that with the addition of AO, IPA, and BQ, the degradation curves decline compared with the no scavenger, indicating that h^+ , $\bullet OH$ and $\bullet O_2^-$ all play a certain role in the degradation process. The degradation rate of MB slightly suppressed in the presence of IPA, which explains that $\bullet OH$

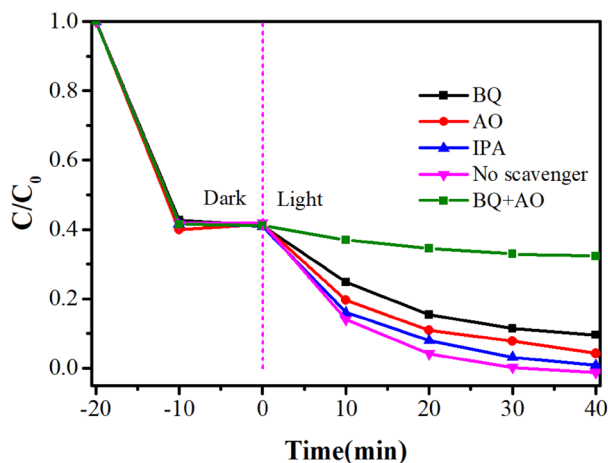


Fig. 8 The trapping experiments of reactive species in the degradation of MB by 30% AW/BMO

is not the main active component. The degradation rate of MB significantly decreased in the presence of the same time of AO and BQ, indicating that h^+ and $\bullet O_2^-$ were the most important active group.

The value band edge (E_{VB}) and conduction band edge (E_{CB}) of AW and BMO could be calculated by the following equation [46, 47]:

$$E_{VB} = X - E_e + 0.5E_g \quad (2)$$

$$E_{CB} = E_{VB} - E_g \quad (3)$$

where X and E_e are the absolute electronegativity (the value of X for AW and BMO was ca. 6.1 and 5.51 eV, respectively [48]) and the energy of free electrons on the hydrogen scale (ca. 4.5 eV). Hence, the E_{CB} and E_{VB} values of AW are 0.05 eV and 3.15 eV and BMO are -0.29 eV and 2.31 eV.

Basing on the above analyses, two possible mechanisms for the photocatalytic degradation of dyes were predicted. As can be seen in Fig. 9a, the CB of BMO is more negative than that of AW, and electrons can be transferred from the CB of BMO to the CB of AW. The VB of AW is more positive than the BMO, and the holes can be transferred from the VB of AW to the VB of BMO. However, the potential for CB of AW (0.05 eV) is more positive than $O_2/\bullet O_2^-$ (-0.046 eV), which indicates that the electrons in CB of AW could not reduce O_2 to $\bullet O_2^-$. This is inconsistent with the results in the capture experiment. Thus, the more reasonable possible mechanism which named a direct Z-scheme is proposed in Fig. 9b. The electrons in CB of AW transfer to the VB of BMO, thereby reducing the internal self-composite of the AW and BMO. The CB of BMO is more negative with a stronger reduction capacity and the VB of AW is more positive with a stronger oxidation capacity, thus has a stronger photocatalytic activity.

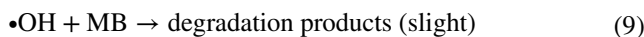
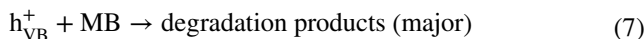
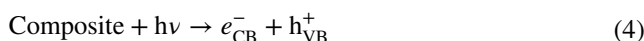
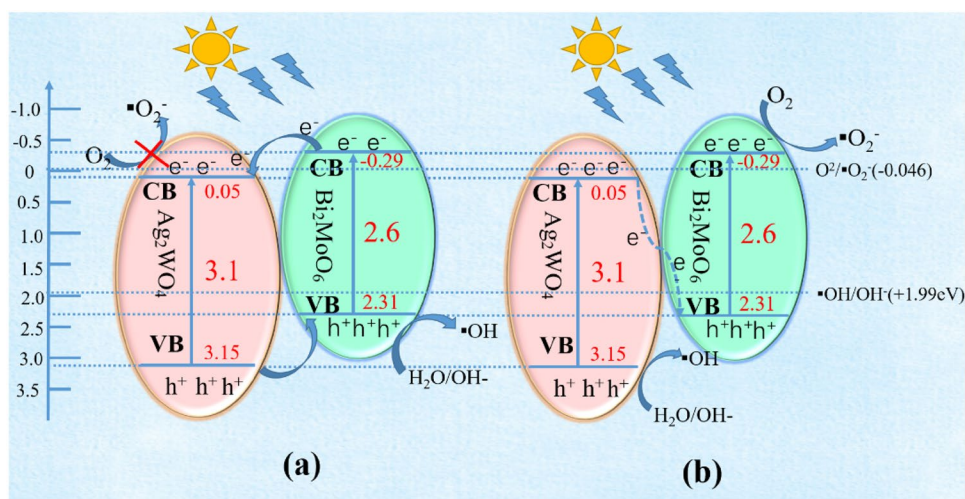


Fig. 9 Possible photocatalytic processes and charge separation of AW/BMO



4 Conclusions

In summary, a series of Z-scheme AW/BMO composites were synthesized by a simple method. Compared with pure AW and BMO, the AW/BMO composites had higher photocatalytic performance, in which 30% AW/BMO sample possessed the highest photocatalytic activity and superior adsorption capability for methylene blue (MB). The degradation rates of pure AW, BMO, 20% AW/BMO, 30% AW/BMO, and 40% AW/BMO composites were 32%, 70%, 94.3%, 100%, and 96% in 30 min. The enhanced photocatalytic activity was due to a synergistic effect in the $\text{Ag}_2\text{WO}_4/\text{Bi}_2\text{MoO}_6$ composites, lower electron–hole recombination, and more electron–hole separation. In addition, radical trapping experiments revealed that the $\bullet\text{O}_2^-$ and h^+ were the main active species in the process of catalytic degradation. The AW/BMO composites provide a higher photocatalytic activity, which shows that AW/BMO is a very promising photocatalyst for organic pollutants remove under visible-light irradiation.

References

1. K. Mukes, Z. Yanfeng, L. Yi-Sheng, H. Anders, G. Jinghua, *Chem. Rev.* **114**, 9662 (2014)
2. C. Chuncheng, M. Wanhong, Z. Jincai, *Soc. Rev.* **39**, 4206 (2010)
3. X. Chen, L. Lei, P.Y. Yu, S.S. Mao, *Science* **331**, 746 (2011)
4. S.U.M. Khan, A.S. Mofareh, W.B. Ingler, *Science* **297**, 2243 (2002)
5. C.M. Nan, J. Bo, C.W.K. Chow, S. Chris, *Water Res.* **44**, 2997 (2010)
6. O.K. Varghese, M. Paulose, T.J. Latempa, C.A. Grimes, *Nano Lett.* **9**, 731 (2009)
7. Q. Yan, X. Xie, Y. Liu, S. Wang, M. Zhang, Y. Chen, Y. Si, *J. Hazard. Mater.* **371**, 304 (2019)
8. L. Xue, H. Jing, S. Jiang, L. Zhe, W. Miao, G. Che, *RSC Adv.* **5**, 104815 (2015)
9. P. Indhumati, J. Himendra, L. Ning, S. Patrik, *Small* **8**, 3073 (2012)
10. F. Chen, Q. Yang, J. Sun, F. Yao, S. Wang, Y. Wang, X. Wang, X. Li, C. Niu, D. Wang, G. Zeng, *ACS Appl. Mater. Interfaces* **8**, 32887 (2016)
11. Y. Liu, J. Kong, J. Yuan, W. Zhao, X. Zhu, C. Sun, J. Xie, *Chem. Eng. J.* **331**, 242 (2018)
12. J. Safaei, H. Ullah, N.A. Mohamed, M.F. Mohamad Noh, M.F. Soh, A.A. Tahir, N. Ahmad Ludin, M.A. Ibrahim, W.N.R. Wan Isahak, M.A. Mat Teridi, *Appl. Catal. B* **234**, 296 (2018)
13. M. Zhou, Z. Guo, Q. Song, X. Li, Z. Liu, *Chem. Eng. J.* **370**, 218 (2019)
14. Z. Liang, C. Zhou, J. Yang, Q. Mo, Y. Zhang, Y. Tang, *Inorg. Chem. Commun.* **93**, 136 (2018)
15. X. Xie, Y. Liu, X. Dong, C. Lin, X. Wen, Q. Yan, *Appl. Surf. Sci.* **455**, 742 (2018)
16. W. Zhang, J. Wang, Y. Yang, Y. Liang, Z. Gao, *J. Colloid Interface Sci.* **531**, 502 (2018)
17. Y. Wang, W. Jiang, W. Luo, X. Chen, Y. Zhu, *Appl. Catal. B* **237**, 633 (2018)
18. R. Hu, X. Xiao, S. Tu, X. Zuo, J. Nan, *Appl. Catal. B* **163**, 510 (2015)
19. X. Wu, Y.H. Ng, X. Wen, H.Y. Chung, R.J. Wong, Y. Du, S.X. Dou, R. Amal, J. Scott, *Chem. Eng. J.* **353**, 636 (2018)
20. H. Li, T. Hu, R. Zhang, J. Liu, W. Hou, *Appl. Catal. B* **188**, 313 (2016)
21. J. Bi, L. Wu, J. Li, Z. Li, X. Wang, X. Fu, *Acta Mater.* **55**, 4699 (2007)
22. Z. Yang, M. Shen, K. Dai, X. Zhang, H. Chen, *Appl. Surf. Sci.* **430**, 505 (2018)
23. S. Yoshiki, K. Hideki, K. Hisayoshi, K. Akihiko, *Cheminform* **37**, 17790 (2006)
24. X. Du, J. Wan, J. Jia, C. Pan, X. Hu, J. Fan, E. Liu, *Mater. Des.* **119**, 113 (2017)
25. J. Zhang, Z. Ma, *J. Taiwan Inst. Chem. Eng.* **88**, 121 (2018)
26. J. Li, Y. Yin, E. Liu, Y. Ma, J. Wan, J. Fan, X. Hu, *J. Hazard. Mater.* **321**, 183 (2017)
27. T. Hu, Y. Yang, K. Dai, J. Zhang, C. Liang, *Appl. Surf. Sci.* **456**, 473 (2018)
28. S. Wang, X. Yang, X. Zhang, X. Ding, Z. Yang, K. Dai, H. Chen, *Appl. Surf. Sci.* **391**, 194 (2017)

29. X. Li, S. Fang, L. Ge, C. Han, P. Qiu, W. Liu, *Appl. Catal. B* **176–177**, 62 (2015)
30. J. Liang, F. Liu, J. Deng, M. Li, M. Tong, *Water Res.* **123**, 632 (2017)
31. Q. Yan, Y. Si, X. Xie, Y. Chen, M. Zhang, *J. Mater. Sci.* **29**, 20866 (2018)
32. Y. Zhao, C. Lin, H. Bi, Y. Liu, Q. Yan, *Appl. Surf. Sci.* **392**, 701 (2017)
33. C. Lin, X. Xie, C. Li, Q. Yan, *Mater. Sci. Semicond. Process.* **82**, 46 (2018)
34. J. Zhang, Z. Ma, *J. Taiwan Inst. Chem. Eng.* **71**, 156–164 (2017)
35. H. Chen, Y. Xu, *Appl. Surf. Sci.* **319**, 319 (2014)
36. Y. Li, Y. Li, S. Ma, P. Wang, Q. Hou, *J. Hazard. Mater.* **338**, 33 (2017)
37. Y.M. Hunge, A.A. Yadav, M.A. Mahadik, V.L. Mathe, C.H. Bho-sale, *J. Taiwan Inst. Chem. Eng.* **85**, 273 (2018)
38. A.A. Yadav, Y.M. Hunge, V.L. Mathe, S.B. Kulkarni, *J. Mater. Sci.* **29**, 15069 (2018)
39. A.A. Yadav, Y.M. Hunge, S.B. Kulkarni, *Ultrason. Sonochem.* **58**, 104663 (2019)
40. Y.M. Hunge, A.A. Yadav, V.L. Mathe, *Chem. Phys. Lett.* **731**, 136582 (2019)
41. Y.M. Hunge, A.A. Yadav, S. Liu, V.L. Mathe, *Ultrason. Sonochem.* **56**, 284 (2019)
42. H. Ym, *MOJ Polym. Sci.* **1**, 135 (2017)
43. X. Xu, L. Hu, N. Gao, S. Liu, S. Wageh, A.A. Al-Ghamdi, A. Alshahrie, X. Fang, *Adv. Funct. Mater.* **25**, 445 (2015)
44. W. Na, H. Cui, S. Qiang, L. Zhang, X. Song, W. Ke, Y. Zhang, L. Jian, W. Jing, T. Jian, *Appl. Catal. B* **198**, 83 (2016)
45. C. Jing, X. Benyan, L. Haili, L. Bangde, C. Shifu, *Dalton Trans.* **41**, 11482 (2012)
46. F. Dong, Y. Sun, M. Fu, Z. Wu, S.C. Lee, *J. Hazard. Mater.* **219–220**, 26 (2012)
47. G. Tian, Y. Chen, X. Meng, J. Zhou, W. Zhou, K. Pan, C. Tian, Z. Ren, H. Fu, *ChemPlusChem* **78**, 117 (2013)
48. J. Lv, K. Dai, J. Zhang, L. Lu, C. Liang, L. Geng, Z. Wang, G. Yuan, G. Zhu, *Appl. Surf. Sci.* **391**, 507 (2017)

Publisher's Note Springer Nature remains neutral with regard to jurisdictional claims in published maps and institutional affiliations.